



Contents lists available at ScienceDirect

## International Journal of Heat and Mass Transfer

journal homepage: [www.elsevier.com/locate/ijhmt](http://www.elsevier.com/locate/ijhmt)

## A 2-D numerical study of chaotic flow in a natural convection loop

El Hassan Ridouane<sup>a,\*</sup>, Christopher M. Danforth<sup>a,b</sup>, Darren L. Hitt<sup>c</sup><sup>a</sup> Department of Mathematics & Statistics, University of Vermont, 16 Colchester Ave., Burlington, VT 05405, USA<sup>b</sup> Complex Systems Center, Vermont Advanced Computing Center, University of Vermont, Burlington, VT 05405, USA<sup>c</sup> Mechanical Engineering Program, School of Engineering, 33 Colchester Ave., University of Vermont, Burlington, VT 05405, USA

## ARTICLE INFO

## Article history:

Received 3 March 2009

Received in revised form 30 September 2009

Available online xxxxx

## Keywords:

Unsteady natural convection

Lorenz chaotic regime

Kelvin–Helmholtz instabilities

## ABSTRACT

This paper numerically investigates the nonlinear dynamics of the unstable convection regime of the thermal convection loop, an experimental analogue of the Lorenz model. The lower half of the toroidal loop is heated and maintained at a constant high temperature, while the upper half is cooled at a constant low temperature. Subject to the proper boundary conditions, the system of governing equations is solved using a finite volume method. The numerical simulations are performed for water corresponding to  $Pr = 5.83$  and Rayleigh number varying from 1000 to 150,000. In the case of a loop heated from below and cooled from above, it has been demonstrated theoretically and experimentally in the literature that multiple flow regimes are possible. Numerical results in terms of streamlines, isotherms, and local heat flux distributions along the walls are presented for each flow regime. Although several studies have investigated the chaotic regime of convection loops, there have been no detailed numerical simulations of the dynamics of flow reversals. Fine-scale flow behavior during the transition from one flow direction to another is illustrated by the temporal evolution of temperature distribution, mass flow rate, and local heat flux at selected locations in the system. Issues related to the observed Kelvin–Helmholtz instabilities are discussed.

© 2009 Elsevier Ltd. All rights reserved.

## 1. Introduction

From fluid physics, when a gas or a single-phase liquid is placed inside a stationary closed space, circulatory convective flow is sustained when a temperature difference is applied at two or more active walls. The state-of-the-art chapters written by Yang [1], Raithby and Hollands [2], and Jaluria [3] disclosed an important subclass of enclosure problems in several branches of engineering, geophysics, environmental sciences, etc. The literature on natural convection in conventional configurations of square and rectangular enclosures is rich, as evidenced by the articles cited in [1–3]. However, less is known about other configurations which are also useful in engineering applications; the thermal convection loop fits into this category. The latter is of remarkable importance as it is widely used in solar water heaters, nuclear reactors, gas turbine blade cooling, and other applications [4,5]. Lorenz's 3-D ordinary differential equation model of convection in a Rayleigh–Bénard cell, a simplified model of this system, has been studied extensively by atmospheric scientists examining the nonlinear error growth observed in sophisticated models of atmospheric convection [6,7].

Thermal convection loops are systems in which fluid motion is induced by buoyancy forces when a temperature difference is ap-

plied at the walls. The fluid circulates in a closed pipe system, heated from below and cooled from above, oriented in a vertical plane. Depending on the density variations, which are directly proportional to the temperature difference between the hot and cold walls, multiple flow regimes are possible. These are pure conduction, steady convective flow that may rotate clockwise (CW) or counter-clockwise (CCW), and Lorenz-like chaotic flow [8]. The most representative studies dealing with this subject are cited chronologically in the following paragraphs. Earlier convection studies used one-dimensional models to mimic the fluid flow and heat transfer in a differentially heated fluid loop assuming that all governing parameters are uniform over a cross section of the system [9,10]. Periodic oscillations were found analytically by Keller [9] in a 1-D model consisting of a fluid-filled tube bent into a rectangular shape and standing in a vertical plane. In a theoretical discussion, Welander [10] found that 1-D systems have one steady solution with warm fluid rising in one branch and cold fluid sinking in the other. This solution may, however, become unstable in an oscillatory manner. A weak instability takes the form of pulsations, while a strong instability takes the form of oscillations with zero mean motion.

A stability study of natural convection was conducted experimentally by Creveling et al. [11] in a glass thermal convection loop filled with water and oriented in a vertical plane. At low and high heat transfer rates the flow was observed to be steady. For an

\* Corresponding author. Tel.: +1 802 656 4595; fax: +1 802 656 1929.  
E-mail address: [eridouan@uvm.edu](mailto:eridouan@uvm.edu) (E.H. Ridouane).

**Nomenclature**

$c_p$	specific isobaric heat capacity, J/kg K	$u, v$	dimensionless velocities in the $x$ - and $y$ -directions
$g$	acceleration of gravity, $m/s^2$	$V$	dimensionless velocity magnitude
$h$	local convective heat transfer coefficient, $W/m^2 K$		
$k$	thermal conductivity, $W/m K$		
$L^*$	gap width, $[=r_o^* - r_i^*]$ , m	<i>Greek letters</i>	
$\dot{m}$	dimensionless mass flow rate, $[=\dot{m}^*/\rho v L^* Gr = \dot{m}^* Pr / \rho v L^* Ra]$	$\alpha$	thermal diffusivity, $[=k/\rho c_p]$ , $m^2/s$
$Nu$	local Nusselt number $[=hL^*/k]$	$\beta$	coefficient of volumetric thermal expansion, $1/K$
$\bar{Nu}$	mean Nusselt number	$\mu$	viscosity, $kg/m s$
$p$	dimensionless static pressure	$\nu$	kinematic viscosity, $[=\mu/\rho]$ , $m^2/s$
$Pr$	Prandtl number, $[=v/\alpha]$	$\rho$	density, $kg/m^3$
$r^*$	torus radius, $[=(r_o^* + r_i^*)/2]$ , m	$\psi$	dimensionless stream function, $[u = \partial\psi/\partial y, v = -\partial\psi/\partial x]$
$r_i^*$	inner radius, m	<i>Subscripts</i>	
$r_o^*$	outer radius, m	$C$	cold wall
$R$	radius ratio, $[=(r_o^* + r_i^*)/L^*]$	$H$	hot wall
$Ra$	Rayleigh number, $[=g\beta(T_H^* - T_C^*)L^{*3}/v\alpha]$	max	maximum value
$t$	dimensionless time, $[=\alpha t^*/L^{*2}]$	<i>Superscript</i>	
$T$	dimensionless temperature	*	dimensional variables
$T_o^*$	reference temperature, $[=(T_H^* + T_C^*)/2]$ , K		

intermediate range, however, the flow was found to be highly oscillatory. Their experimental observations agreed with the theoretical analyses by Keller [9] and Welander [10]. Gorman et al. [12] presented a quantitative comparison of the flow in a thermal convection loop with the nonlinear dynamics of the Lorenz model. Their model was heated at constant heat flux over the bottom half and cooled at a constant temperature over the top half. The boundaries of different flow regimes were determined experimentally and the characteristics of chaotic flow regimes were discussed. They also derive a relationship between the parameters of the Lorenz model and the experimental parameters of the fluid and loop.

In a theoretical and experimental investigation, Yuen and Bau [13] used optimal control theory to construct a controller to suppress chaotic flow regimes in a thermal convection loop. This technique is often used in many industrial processes to maintain desirable flow conditions. The authors demonstrated, in both experiments and theory, that the nature of the flow in a thermal convection loop heated from below and cooled from above can be significantly modified and that chaos can be controlled. On a related topic, Tang and Bau [14–18] studied analytically and experimentally the stabilization of the flow in Rayleigh–Bénard convection using feedback controllers. With the aid of a controller, they showed that the transition from no-motion to steady convection can be significantly postponed.

The stability of single-phase loops has been the subject of investigation by Vijayan and Austregesilo [19]. Scaling laws were developed and successfully verified against experimental data using various loops. The stability behavior of uniform diameter loops can be expressed in terms of non-loop dimensionless groups of parameters. These correlations have recently been extended to loops with non-uniform diameters by Vijayan [20]. Jiang et al. [21] studied the effects of boundary conditions on flow stability in a thermal convection loop. The experiment was performed on a copper torus and the observations were in contrast with those reported on a glass torus. The Lorenz-like chaotic flow was not observed and the authors attributed this to the fact that the high thermal conductivity of the walls deforms the heat flux distribution and hence affects the global flow stability. Jiang and Shoji [22] also focused their study on the influence of thermal boundary conditions on the spatial and temporal stabilities of the flow. Multi-scale analysis was applied to study the flow fluctuation and self-organization in a thermal convection loop. In the analysis, a coefficient

was proposed to measure the differences in thermal boundary condition. Depending on the value of this coefficient, spatial and/or temporal instabilities may occur leading to Lorenz-like or intermittent chaos.

Lavine et al. [23,24] reported the outcome of a numerical study of natural convection assuming steady-state conditions and flow symmetry about the vertical plane. The study was undertaken in two distinct parts. In the first part [23], the Grashof number was fixed at 1900 and the effect of a tilted angle varying between  $0^\circ$  and  $90^\circ$  was investigated. It was shown that the flow is strongly three dimensional and the friction factor is higher than for fully developed laminar flow in a straight pipe. Regions of streamwise flow reversals were predicted for low tilt angle causing the total buoyancy to decrease. In the second part [24], results were presented for two different Grashof numbers exhibiting flow regimes, which have been experimentally observed at higher Grashof numbers such as flow reversals and secondary motions. The strength of these flows is greater for the higher Grashof number and the total buoyancy decreases with increasing Grashof number. Burroughs et al. [25] numerically analyzed the flow in the loop at low Grashof number for a wide range of Prandtl number using a Fourier–Chebyshev spectral method. The numerical results were found to converge toward the asymptotic results of coupled nonlinear PDEs developed by the authors to describe the flow in the loop.

Despite the wealth of literature for this problem, there is little information on the spatiotemporal details of the flow and only three studies have been identified. Ambrosini et al. [26] focused on 1-D stability analysis of single-phase circulation in a rectangular loop at the transition from laminar to turbulent. They found that the choice of a friction law has an important effect on the numerical predictions. Recently, Pikhwal et al. [27] used CFD code to model 1-D and 3-D circulation in a rectangular loop made of glass under different heating/cooling configurations. The 3-D model showed the origin of pulsating instabilities observed in the experiments when the loop is heated from below and cooled from the top. Desrayaud et al. [8] recently investigated numerically the unsteady laminar natural convection in a 2-D loop maintained at a constant heat flux over the bottom half and cooled at a constant temperature over the top half. Their results were presented for a relatively wide loop with radius ratio  $R = 3$ . In contrast, the objective of this paper is to perform direct unsteady numerical simulations of laminar natural convection in a loop with the torus radius

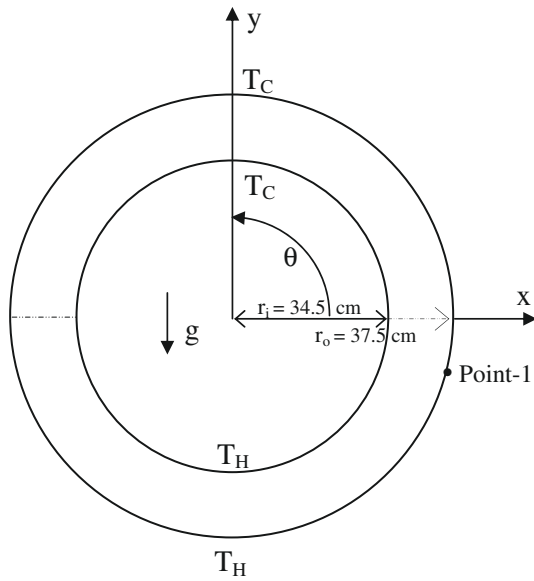


**Fig. 1.** Schematic of the thermal convection loop (not drawn to scale). The dimensions of the loop are 34.5 cm inner radius and 37.5 cm outer radius, giving a radius ratio  $R$  of 24. The exterior of the lower half is heated and maintained at a constant high temperature  $T_H$ , while the exterior of the upper half is cooled at a constant low temperature  $T_C$ .

much larger than the pipe radius ( $R = 24$ , see Fig. 1). Details of the flow behavior accompanying the transitions taking place as the flow reverses direction during the chaotic regime were revealed for the first time by presenting the temporal evolution of the flow structure during these transitions, and by providing the time history of the mass flow rate and local heat flux at selected locations in the system. The simulations are now described in greater detail.

## 2. Model of the physical system and numerical methods

The physical system consists of a circular loop filled with water and oriented in a vertical plane as shown in Fig. 1. The dimensions of the loop are 69 cm inner diameter and 75 cm outer diameter, giving a radius ratio  $R$  of 24. Initially, the water is in thermal equilibrium at  $T_0^* = 300$  K. At a preset time, the lower ( $\theta = \pi$  to  $2\pi$ ) wall is heated and maintained at a high temperature  $T_H^* = 310$  K while the upper ( $\theta = 0$  to  $\pi$ ) wall is cooled and maintained at a low temperature  $T_C^* = 290$  K. Temperature discontinuities between the hot and cold walls at  $\theta = 0$  and  $\pi$  were avoided by a smooth linear transition from  $T_H^*$  to  $T_C^*$  over a small distance  $\varepsilon = 0.8$  cm around  $\theta = \pi$  and  $\theta = 2\pi$ . In all numerical results presented, a constant temperature differential ( $T_H^* - T_C^*$ ) of 20 K is imposed between the hot and cold walls, changes to the Rayleigh number were made by adjusting gravity. For this modest temperature differential we regard the variations of all material properties with temperature to be negligible. Correspondingly, the standard Boussinesq approximation is adopted and all fluid properties are assumed to be constant and evaluated at the reference temperature  $T_0^*$ . To justify this assumption, steady-state cases with temperature-dependant fluid properties were conducted and very small deviations of less than 0.4% were observed in the mass flow rate and the mean wall heat flux. The fluid flow is assumed to be laminar, two dimensional, and the viscous dissipation is neglected due to low velocities. Under these circumstances, the governing dimensionless equations are the unsteady, 2-D laminar Navier–Stokes equations along with the energy equation:

$$\frac{\partial u}{\partial x} + \frac{\partial v}{\partial y} = 0 \quad (1)$$

$$\frac{\partial u}{\partial t} + u \frac{\partial u}{\partial x} + v \frac{\partial u}{\partial y} = -\frac{\partial p}{\partial x} + Pr \left( \frac{\partial^2 u}{\partial x^2} + \frac{\partial^2 u}{\partial y^2} \right) \quad (2)$$

$$\frac{\partial v}{\partial t} + u \frac{\partial v}{\partial x} + v \frac{\partial v}{\partial y} = -\frac{\partial p}{\partial y} + Pr \left( \frac{\partial^2 v}{\partial x^2} + \frac{\partial^2 v}{\partial y^2} \right) + Ra Pr T \quad (3)$$

$$\frac{\partial T}{\partial t} + u \frac{\partial T}{\partial x} + v \frac{\partial T}{\partial y} = \left( \frac{\partial^2 T}{\partial x^2} + \frac{\partial^2 T}{\partial y^2} \right) \quad (4)$$

The dimensionless variables in the above equations are defined as

$$t = \frac{t^* \alpha}{L^{*2}}, \quad x = \frac{x^*}{L^*}, \quad y = \frac{y^*}{L^*}, \quad u = \frac{u^* L^*}{\alpha}, \quad v = \frac{v^* L^*}{\alpha},$$

$$p = \frac{p^* L^{*2}}{\rho \alpha^2}, \quad T = \frac{(T^* - T_C^*)}{(T_H^* - T_C^*)}. \quad (5)$$

In the above equations,  $\rho$ ,  $T$ , and  $\alpha$  represent the density, dimensionless temperature, and thermal diffusivity. The superscript  $*$  in Eq. (5) indicate the dimensional variables. The velocity field is subject to no-slip boundary conditions. Prescribed constant temperature boundary conditions of  $T_H^*$  and  $T_C^*$  are imposed at the heated bottom and cooled upper walls, respectively. The laminar nature of the flow has been verified at the highest Rayleigh number of 150,000 which produces chaotic oscillations with flow reversals. The maximum Reynolds number calculated using the largest observed value of the mass flow rate was  $Re_{max} = 210.5$ .

The computational domain is constructed to be coincident with the physical domain forming the circular loop with no symmetry assumptions. The governing Eqs. (1)–(4), subject to the boundary and initial conditions, are solved using the finite volume method. An implicit segregated solver is used and all discretization schemes employed are of second-order accuracy or higher. The QUICK scheme is used for the momentum, energy and density discretization. A second-order body-force-weighted scheme is used in the pressure discretization and the SIMPLE scheme is used in the pressure–velocity coupling. Convergence of a simulation at each time step was assessed through the monitoring of computed residuals (velocity, energy, and mass conservation) and also through the convergence of point and/or surface monitors for velocity, temperature and heat flux at selected locations in the domain by setting their absolute convergence criterion to  $10^{-6}$ . The numerical simulations are performed for water corresponding to  $Pr = 5.83$ , and Rayleigh number varying from 1000 up to 150,000, using the commercial software FLUENT 6.3 [28].

A grid independence study was conducted in the steady-state convection regime at  $Ra = 8 \times 10^4$ . Based on a sequence of numerical experiments using various grid sizes ranging from 7500 up to 78,000 quadrilateral elements, it was found that a uniform mesh constructed with 16,890 finite volume quadrilateral elements provided a good compromise between the computational efforts and accuracy. Table 1 illustrates the effect of the grid size on the solution. Grid independence was achieved within one percent of the maximum velocity magnitude, the mass flow rate, as well as the mean Nusselt number at both the hot and cold walls. A section

**Table 1**

Effect of grid size on the steady-state solution at  $Ra = 80,000$ . Based on a sequence of numerical experiments, the optimal computational mesh is constructed with 16,890 finite volume quadrilateral elements (see Fig. 2). Grid independence was achieved within one percent of the maximum velocity magnitude, the mass flow rate as well as the heat transfer rate at the walls.

Mesh	$V_{max}$	$\overline{Nu}_H$	$\overline{Nu}_C$	$\dot{m}$
7500	747.74	2.127	-2.127	0.1540
16,890	747.74	2.105	-2.105	0.1554
30,000	749.77	2.103	-2.103	0.1556
78,000	751.81	2.105	-2.105	0.1562

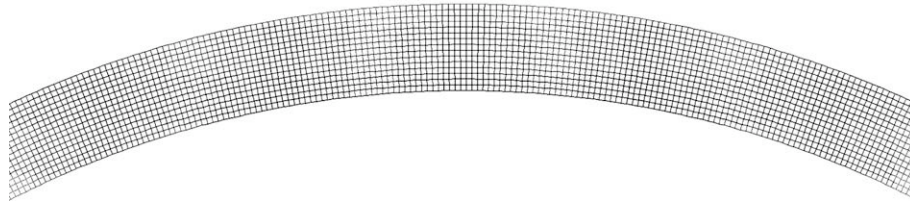


**Fig. 2.** Portion of the computational grid showing the distribution of elements within the loop. Based on a sequence of numerical experiments, the optimal computational mesh is constructed with 16,890 finite volume quadrilateral elements. Grid independence was achieved within one percent of the maximum velocity magnitude as well as the mean wall heat flux at the walls.

of the computational grid employed and composed entirely of orthogonal elements is shown in Fig. 2.

Validation of the computer code used to predict the velocity and temperature fields was performed in a differentially heated wide loop of radius ratio  $R = 1.75$  in order to compare with published data. The computed mean Nusselt number is compared against the results published in Kuehn and Goldstein [29] and Desrayaud et al. [8] using air as the working fluid in Table 2. Good agreement was observed in the range of the Rayleigh number under consideration, with the maximum difference being less than one percent.

### 3. Results and discussion

In the case of a loop heated from below and cooled from above, it has been demonstrated theoretically and experimentally [8,10,11,21] that multiple flow regimes are possible in the range of Rayleigh number considered in the present work. These are pure conduction, steady convective flow that may rotate CW or CCW by chance, and Lorenz-like chaotic flow. Numerical results in terms of

streamlines, isotherms, and local heat flux along the walls are presented for each flow regime. A special effort is devoted to illustrate how the flow reversals occur during the Lorenz-like chaotic regime. This is done by presenting the temporal evolution of the flow structure during the transition from one flow direction to another, and by providing the time history of the mass flow rate and local heat flux at selected locations in the system. Also, issues related to the observed Kelvin–Helmholtz instabilities are discussed.

#### 3.1. Conduction regime

The first solution obtained for a small forcing ( $Ra = 1000$ ) is illustrated in Fig. 3. This solution has been generated by maintaining the walls along the lower half of the system at a high temperature  $T_H^*$  and the walls along the upper half at a low temperature  $T_C^*$ , while the fluid was initially in thermal equilibrium at  $T_0^* = (T_H^* + T_C^*)/2$ . At this value of  $Ra$ , the system is initialized slightly above the critical  $Ra$  value corresponding to the onset of thermal convection. The fluid motion is very slow and consists of eight counter rotating cells. The small circulations are limited to the regions where the temperature discontinuity occurs. Four counter rotating cells exist at the left discontinuity and four at the right discontinuity. The remaining fluid along the loop is motionless and it is observable that this solution is symmetric with respect to the center of the loop. The temperature field is characterized by a dominant conductive mode and consequently the fluid is hot in the lower half and cold in the upper half with small regions exhibiting temperature gradients near the discontinuities. The convective motion is oriented upward for the two upper cells and downward for the lower cells.

**Table 2**

Comparison of the mean Nusselt number in a differentially heated loop against the results of Kuehn and Goldstein [29] and Desrayaud et al. [8]: radius ratio  $R = 1.75$  and  $Pr = 0.7$  (air).

$Ra$	Kuehn and Goldstein [29]	Desrayaud et al. [8]	Present work
$10^3$	1.081	1.109	1.093
$10^4$	2.010	2.004	2.020
$5 \times 10^4$	3.024	3.031	3.041

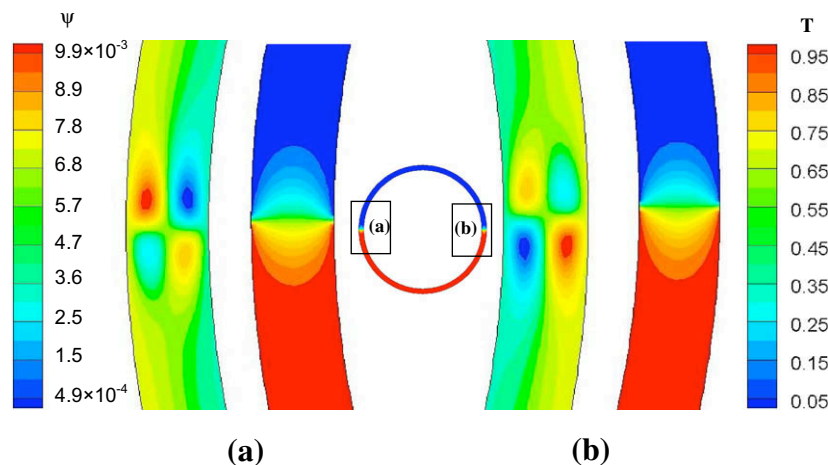


**Fig. 3.** Streamlines (left) and isotherms (right) during the pure conduction regime at  $Ra = 1000$ : (a) left side of the loop near  $\theta = \pi$  and (b) right side of the loop near  $\theta = 0$ . The fluid motion is very slow and consists of eight counter rotating cells. The small circulations are limited to the regions where the temperature discontinuity occurs. Four counter rotating cells exist at the left discontinuity and four at the right discontinuity. The remaining fluid along the loop is motionless and symmetric with respect to the center of the loop. The temperature field is characterized by a dominant conductive mode and consequently the fluid is hot in the lower half and cold in the upper half with small regions exhibiting temperature gradients near the discontinuities.

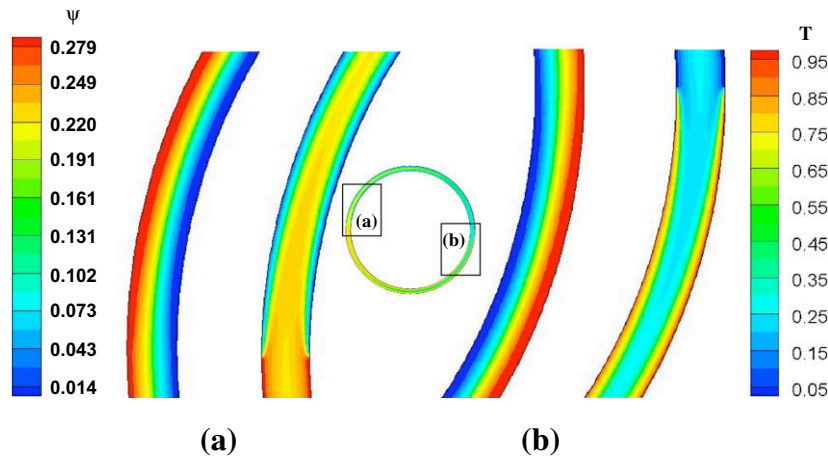


**Fig. 4.** Structure of the steady-state solution showing streamlines (left) and isotherms (right) at  $Ra = 25,000$ : (a) hot fluid flowing through the cold region of the system and (b) cold fluid flowing through the hot region of the system. Fig. 4a and b shows the development of the thermal boundary layer along the walls as the hot/cold stream first encounters the cold/hot walls, respectively. Due to the symmetry of the physical system and boundary conditions, the image of this solution through a vertical plane mirror is also a solution. Both solutions transfer the same amount of heat through the loop, but rotate in opposite directions.

The heat transfer results (not presented here) for this forcing are typical of a dominant conduction regime. In fact, the local Nusselt number,  $Nu$ , along the walls begins with a relatively large value at the points where the discontinuities occur.  $Nu$  exhibits a positive concave U-shape with zero values as we move away from the discontinuities.

### 3.2. Steady convection

When increasing  $Ra$  above 1000, no visible qualitative changes were observed in the cell shapes. Quantitatively however, the intensity of the flow increases, improving the overall heat transfer through the walls of the loop. The buoyant cellular flow is steady for a wide range of  $Ra$ , but as  $Ra$  was gradually increased the cellular patterns disappeared, and a fluid circulation along the loop appears and remains steady. The features of this new steady-state are depicted in Fig. 4 in terms of streamlines (left) and isotherms (right) at  $Ra = 25,000$ . Figs. 4a and b show the development of the thermal boundary layer along the walls as the hot/cold stream first encounters the cold/hot walls, respectively. Due to the symmetry of the physical system and boundary conditions, the image of this solution through a vertical plane mirror is also a solution. Both solutions transfer the same amount of heat through the loop, but rotate in opposite directions.

Illustrated in Fig. 5 is the variation of the local Nusselt number,  $Nu$ , along the outer hot wall from left ( $\theta = \pi$ ) to right ( $\theta = 2\pi$ ) for different values of the Rayleigh number. The fluid motion is steady and rotates CW for the three values of  $Ra$  considered. The lower  $Nu$  curve representative of  $Ra = 10,000$  presents a monotonic increase with respect to the dimensionless distance along the wall beginning with a low value at  $\theta = \pi$  and ending with a high value at  $\theta = 2\pi$ . The large  $Nu$  values in the vicinity of  $\theta = 2\pi$  can be attributed to vigorous convective heat transfer as the cold fluid descending from the upper region of the system first encounters the hot wall. When  $Ra$  is increased to 25,000, the  $Nu$  curve moves up slightly but remains almost parallel for more than three quarters of the distance along the wall. However, the separation between both curves shrinks and the two curves eventually coincide approaching the discontinuity at  $\theta = 2\pi$ . A different behavior is encountered at high  $Ra$  of 80,000. The Nusselt curve is also shifted up with respect to the  $Nu$ -curve related to  $Ra = 25,000$ , but as we approach  $\theta = 2\pi$ ,  $Nu$  develops wave-like patterns before increasing to its high value at the end of the wall.

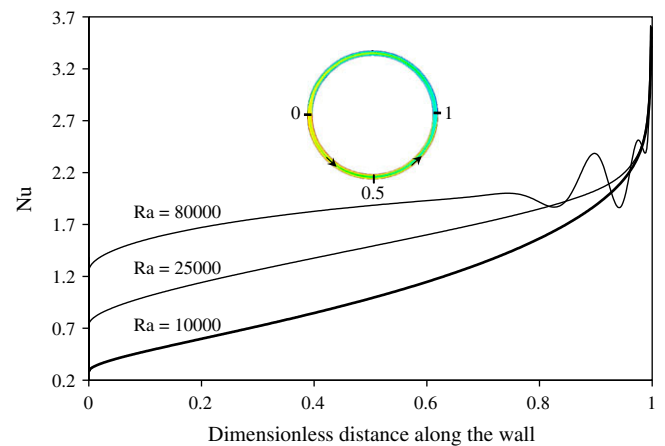


**Fig. 5.** Local Nusselt number along the outer hot wall from left ( $\theta = \pi$ ) to right ( $\theta = 2\pi$ ) at different values of the Rayleigh number. The flow is under steady-state convection for the three values of  $Ra$  considered. The heat Nusselt curves represent a nearly monotonic increase with respect to the dimensionless distance along the wall beginning with a low value at  $\theta = \pi$  and ending with a high value at  $\theta = 2\pi$ . The large  $Nu$  values in the vicinity of  $\theta = 2\pi$  can be attributed to vigorous convective heat transfer as the cold fluid descending from the upper region of the system first encounters the hot wall. A different behavior is encountered at high  $Ra$  of 80,000. The Nusselt curve is shifted up with respect to the  $Nu$ -curve related to  $Ra = 25,000$ , but as we approach  $\theta = 2\pi$ ,  $Nu$  develops wave-like patterns before increasing to its high value at the end of the wall.

It is well known that in Rayleigh–Bénard problems, natural convection becomes oscillatory when the Rayleigh number exceeds a certain critical value. Above this critical value, the steady-state convective motion becomes oscillatory even if the initial conditions are those of a steady-state solution, i.e. steady convection is an unstable solution. Fig. 6 presents the temporal evolution of the mass flow rate at  $Ra = 110,000$ . To ensure that the nature of the oscillations is sustained, the time integration was continued up to  $t = 32.7$ . The fluid is flowing in the CW direction, as the values of the mass flow rate,  $\dot{m}$ , are always positive. A close look at Fig. 6 shows cycles of constant time period where the fluid speeds up and slows down with seemingly random but bounded amplitude. A further increase in the Rayleigh number has no effect on the nature of the oscillations until the flow patterns reach a new state characterized by oscillations with increasing amplitude, followed by flow reversals. This new state, referred to as the Lorenz-like chaotic regime, is discussed in the following section.

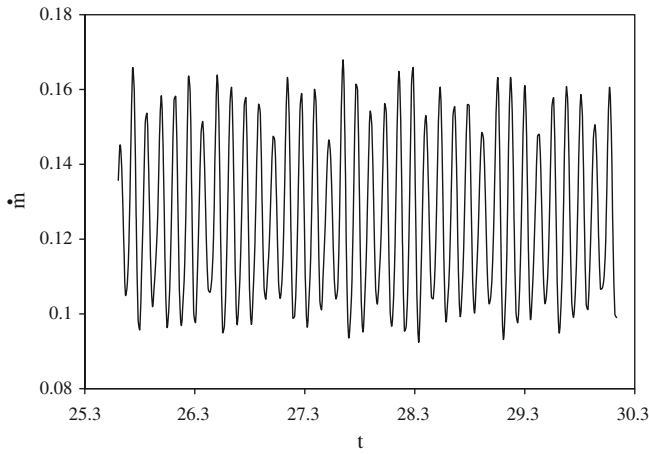


**Fig. 6.** Temporal evolution of the mass flow rate at  $Ra = 110,000$ . The fluid is flowing with seemingly random flux deviations around the loop in the CW direction ( $\dot{m} \geq 0$ ). The figure shows cycles of constant time period where the fluid speeds up and slows down with chaotic bounded amplitude.

### 3.3. Lorenz-like chaotic flow

The temporal evolution of the mass flow rate at  $Ra = 150,000$  is illustrated in Fig. 7, which depicts a typical variation of the  $x$  variable in the original three-variable Lorenz model. The flow undergoes a change in direction each time the mass flow rate  $\dot{m}$  changes sign. Positive values of  $\dot{m}$  correspond to CW rotation, while negative values indicate CCW rotation. The flow rate oscillates with increasing magnitude until it reaches a critical amplitude (as measured from the unstable steady convective solution which appears to be near  $\pm 0.21$ ) leading the flow to change direction. Upon a change in direction, a new cycle begins with a new series of oscillations. It is important to point out that if the magnitude of the first peak in a given direction is large enough, the flow reverses direction quickly without further increases in oscillation amplitude.

Creveling et al. [11] proposed the following positive feedback mechanism to explain these flow reversals. Assume the fluid is in an equilibrium state of CCW flow and that an anomalous warm pocket of fluid arrives at  $\theta = 0$ . The hot pocket exerts a buoyant

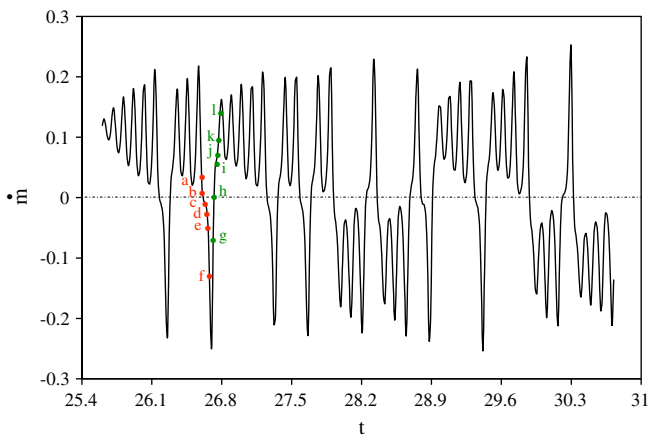


**Fig. 7.** Temporal evolution of the mass flow rate at  $Ra = 150,000$ . The fluid undergoes a flow reversal each time the mass flow rate  $\dot{m}$  changes sign. Positive values of  $\dot{m}$  indicate CW fluid rotation, while negative values indicate CCW rotation. The flow rate oscillates with increasing magnitude until it reaches a critical amplitude leading the flow to change direction. Upon a change in direction, a new cycle begins with a new series of oscillations. If the magnitude of the first peak is large enough, the flow reverses direction quickly without further oscillations.

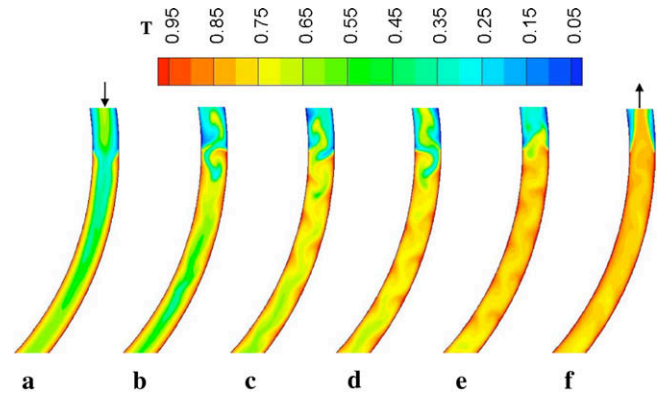


**Fig. 8.** Temporal evolution of the flow structure during the transition from CW to CCW fluid rotation at  $Ra = 150,000$ . Isotherms are plotted at selected times corresponding to instants a–f in Fig. 7. These instants are marked with red dots on the second negative peak in Fig. 7. Slight flow deformations are observed in the vicinity of the temperature discontinuity (a), which take the form of two small circulations. These cells propagate CW along the wall and new cells with higher intensity are created at the discontinuity (b). This Kelvin–Helmholtz like instability intensifies with time as the fluid velocity drops significantly (c). As the system reaches a motionless state with a zero flow rate, a hot stream rises and pushes the cold fluid towards the upper region of the system (e) leading to a new unsteady-state characterized by CCW flow (f).

force on the fluid, causing a positive acceleration in the CCW direction and speeding up the rotation. This pocket cools less on its journey across the top half of the tube, arriving at  $\theta = -\pi$  hotter than it was in its prior trip through the discontinuity. Consequently, there is a buoyant force in the reverse (CW) direction acting to slow down the speed of rotation. The fluid decelerates, but continues in the CCW direction, allowing the anomalous pocket more time to heat up. Upon arriving again at  $\theta = 0$ , the pocket is once again hotter than it was previously, by a greater amount now than before. The buoyant force acting to accelerate the flow is greater this time, since the instability has been magnified. With even less time to cool off as the pocket crosses the top half of the tube, the instability continues to grow, decelerating the clockwise flow again at  $\theta = -\pi$ , etc. Amplification continues until the buoyant force generated by the pocket at  $\theta = -\pi$  grows large enough, causing the flow to stop. With no rotation in the tube, the temperature gradient

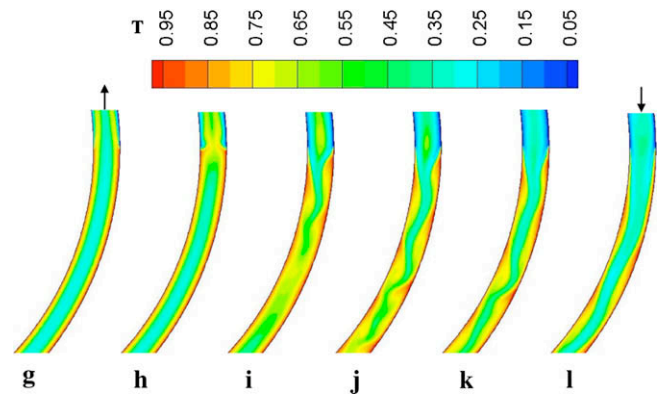


**Fig. 9.** Temporal evolution of the flow structure during the transition from CCW to CW fluid rotation at  $Ra = 150,000$ . Isotherms are plotted at selected instants g–l marked with green dots on Fig. 7. The image at the instant g shows a fast moving CCW flow with no signs of transition. About 40 s later ( $\Delta t = 0.007$ ), two hot streams are diverted from the walls in the region where the temperature discontinuity occurs (h). This deformation propagates CW along the hot wall with longer wavelength and shorter amplitude structures when compared to the transition illustrated in Fig. 8. The secondary flow cells are washed off gradually by the main stream and eventually disappear completely in favor of a new fast moving CW flow (l).

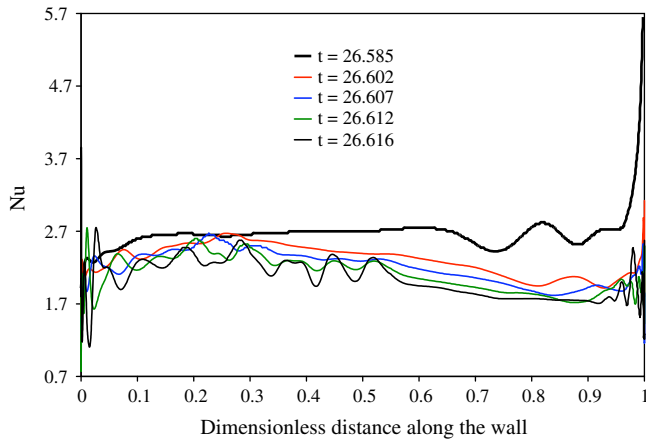


**Fig. 10.** Local Nusselt number along the outer hot wall from left ( $\theta = \pi$ ) to right ( $\theta = 2\pi$ ) at  $Ra = 150,000$ . Each curve illustrates the distribution of the Nusselt number at a typical instant  $t$  during the flow reversal from CW to CCW fluid rotation at early stages of the process. The  $Nu$  curve at  $t = 26.585$  presents the highest heat flux through the wall with a relatively smooth curve compared to the subsequent instants during the process. This is attributed to high fluid velocities at this instant. The signs of a transition were first observed at  $t = 26.602$ , which are manifested in the appearance of small waves at the vicinity of the temperature discontinuities. These waves propagate along the wall and their number and magnitude are directly proportional to the number of secondary cells in contact with the wall.

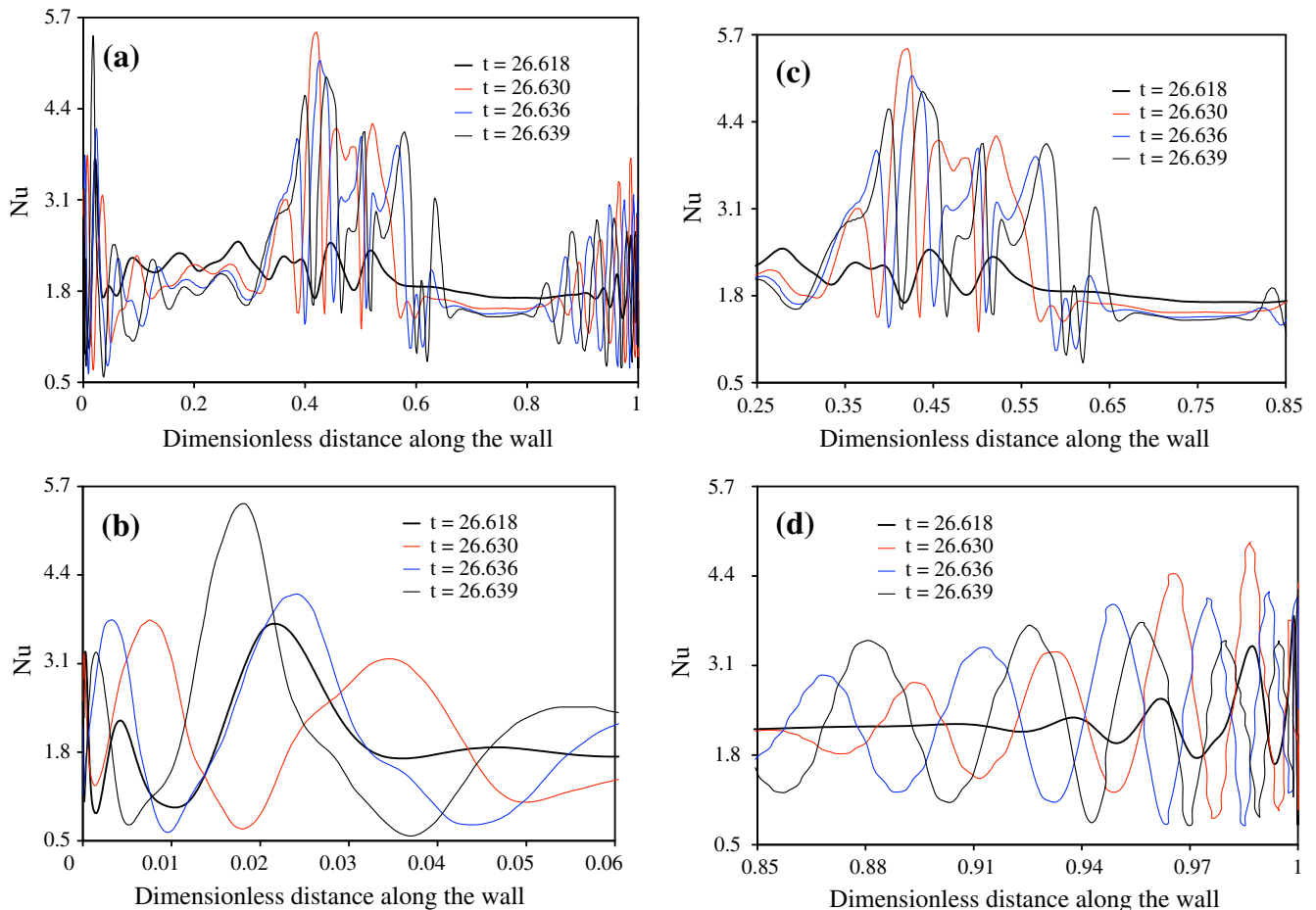


**Fig. 11.** Local Nusselt number along the outer hot wall from left ( $\theta = \pi$ ) to right ( $\theta = 2\pi$ ) at  $Ra = 150,000$ . Each curve illustrates the distribution of the Nusselt number at an intermediate typical instant  $t$  during the flow reversal from CW to CCW fluid rotation: (a) along the entire wall and (b–d) zoom-in images over different segments of the wall. This figure is a continuation of Fig. 10 showing how the subsequent events during the transition affect the Nusselt distribution at the wall. A very complex distribution characterized by long waves is observed. These waves propagate in an organized fashion from left to right (CCW).

between the top and bottom portions of the fluid grows undisturbed. The fluid will then ‘choose’ a direction of rotation and repeat the behavior indefinitely. Of course, when differential heating is below the critical value, these thermal anomalies decay in time.

Flow behavior during the transition from CW to CCW is presented in Fig. 8. Isotherms are plotted at selected times corresponding to instants a–f in Fig. 7. These instants are marked with red dots on the second negative peak in Fig. 7 and more precisely during the decrease of  $\dot{m}$  from a maximum value towards its minimum. At a time  $t = 26.602$ , Fig. 8a reveals that the flow is still rotating CW with a relatively high velocity. Slight flow deformations are observed in the vicinity of the temperature discontinuity, which take the form of two small circulations. These cells propagate CW along the wall and new cells with higher intensity are created at the discontinuity (Fig. 8b). These patterns resemble the Kelvin–Helmholtz instabilities observed when a velocity shear is present within a continuous fluid, or at the interface of two fluids of different densities and velocities [30]. These structures intensify with time once the fluid velocity has dropped significantly indicating the onset of a flow reversal (Fig. 8c). As the system reaches a motionless state with a zero flow rate, a hot stream rises and pushes the cold fluid towards the upper region of the system (Fig. 8e). The thermal anomalies propagate CW and grow in magnitude until the flow pattern reaches a new unsteady-state characterized by CCW flow as depicted in Fig. 8f.

The temporal evolution of the flow structure during another transition is presented in Fig. 9 to complete the visualization of the flow behavior during a full flow cycle. This transition, which takes place as the flow reverses from CCW to CW, also corresponds to the second negative peak in Fig. 7. Isotherms are plotted at selected instants g–l, marked with green dots (Fig. 7), when the flow rate increases crossing the zero value heading towards a maximum. The isotherms in Fig. 9g show a fast moving CCW flow, which occurs roughly 300 s ( $\Delta t = 0.05$ ), after the last image in Fig. 8. Two hot streams are diverted from the walls in the region where the temperature discontinuity occurs as  $t$  increases to the instant h (Fig. 9h). With help from the cold stream descending from the upper region of the loop, this deformation propagates along the hot wall in relatively small structures when compared to the transition illustrated in Fig. 8. The flow reversal during this transition occurs about four times faster than the first flow reversal of Fig. 8. The secondary flow cells are washed off gradually with time by the main stream and eventually disappear completely in favor of a new fast moving CW unsteady-state.

The local Nusselt number,  $Nu$ , along the outer hot wall from left ( $\theta = \pi$ ) to right ( $\theta = 2\pi$ ) is shown in Fig. 10 at  $Ra = 150,000$ . Each curve illustrates the distribution of  $Nu$  at a typical instant  $t$  during the early times of the flow reversal from CW to CCW flow. When examining Fig. 10 we see that the instant  $t = 26.585$  presents the highest heat flux through the wall with a relatively smooth curve compared to the subsequent instants during the process. This is attributed to high fluid velocities at this instant, which occurs near 100 s ( $\Delta t = 0.0163$ ) before the beginning of the transition leading to a flow reversal. A similar trend was reported in Fig. 5 during steady-state convection at  $Ra = 80,000$ . The signs of a transition were first observed at  $t = 26.602$ , manifested in the appearance of small waves at the vicinity of the temperature discontinuities. These waves propagate along the wall and their number and magnitude are directly proportional to the number of secondary cells in contact with the wall. Further increments in time show that the values of  $Nu$  shift down as a result of decreasing fluid velocities.

This behavior intensifies with time while moving towards a motionless state just before the flow reverses direction. The secondary cells multiply in number and magnitude, and as a direct consequence the distribution of the heat flux along the wall becomes more complex. This situation is depicted in Fig. 11 at typical times during the flow reversal. This figure is a continuation of Fig. 10 showing how the subsequent events during the transition affect the heat flux distribution at the wall. For a better visualization, Figs. 11b–d illustrate zoom-in images over different segments of the wall. Regarding the instant  $t = 26.618$ ,  $Nu$  presents a similar trend as in the last instant  $t = 26.616$  of Fig. 10. This is due to the short time period between these two events. The behavior 72 s ( $\Delta t = 0.0118$ ) later was accompanied by a very complex distribution characterized by long waves in the central region of the wall and also near the discontinuities at both ends of the wall. These waves propagate in an organized fashion from left to right (CCW) and seem to predict the next direction of the flow after the transition.

Until now, the results discussed during the chaotic regime, and more precisely during the transitions leading to flow reversals, were provided as a sequence of discrete events during the process. To have a better understanding of the flow behavior during the chaotic regime, a continuous sequence of events in time is required. This is presented in terms of the time history of the local Nusselt number,  $Nu$ , at point-1, which is located on the hot wall around  $\theta = -\pi/6$  (see Fig. 1). The selection of point-1 is based on the interesting events occurring in this particular location as witnessed in Figs. 8 and 11. Fig. 12a shows the temporal evolution of  $Nu$  at point-1 along with the mass flow rate,  $\dot{m}$ , at  $Ra = 150,000$  during flow cycles when the fluid spends more time

oscillating CW. Likewise, Fig. 12b depicts the evolution of the same variables during flow cycles when the fluid spends more time oscillating CCW. Despite the random nature of  $Nu$  variations, it is clearly observed from the figures that the  $Nu$  curve lies almost always above  $\dot{m}$  curve. We suspect this is because when  $\dot{m}$  increases, the fluid velocities intensify and result in a larger heat flux at the wall. Other interesting information that may be extracted from Fig. 12 is related to the organized  $Nu$  oscillations happening each time the flow undergoes a change in direction from CW ( $\dot{m} \geq 0$ ) to CCW ( $\dot{m} \leq 0$ ). The higher the magnitude of these oscillations the larger the negative peak of  $\dot{m}$  becomes.

In summary, Fig. 13 shows the bifurcation diagram illustrating the transitions of the flow with Rayleigh number. Five different flow regimes were encountered in the thermal convection loop as  $Ra$  increases. The maximum error  $\Delta Ra$  associated with each transition is also provided. The flow regimes encountered in this study are consistent with the theoretical studies and experimental observations available in the literature [8–12,20]. The instabilities leading the flow to change direction are real and have been observed in the laboratory by several groups. In fact, as the Rayleigh number increases well beyond the transition from stable to unsta-

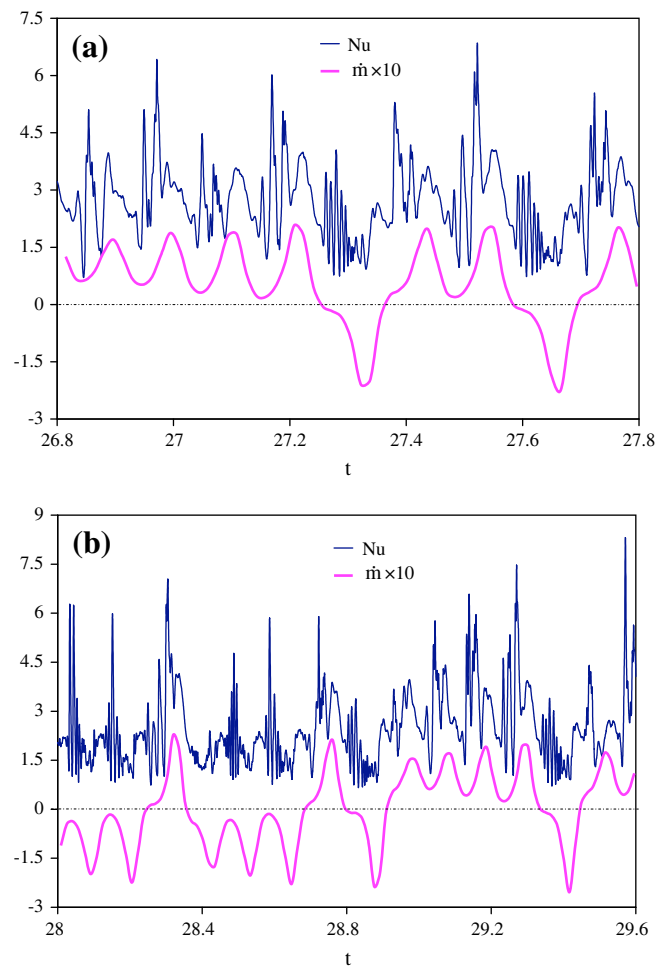


**Fig. 12.** Time history of the local Nusselt number at point-1 along with the mass flow rate at  $Ra = 150,000$ : (a) flow cycles when the fluid spends more time oscillating CW and (b) flow cycles when the fluid spends more time oscillating CCW. Despite the random nature of  $Nu$  variations, it is clearly observed from the figures that the  $Nu$  curve lies almost always above  $\dot{m}$  curve. We suspect this is because when  $\dot{m}$  increases, the fluid velocities intensify and result in a larger heat flux at the wall. Organized  $Nu$  oscillations are observed each time the flow undergoes a change in direction from CW ( $\dot{m} \geq 0$ ) to CCW ( $\dot{m} \leq 0$ ). The higher the magnitude of these oscillations the larger the negative peak of  $\dot{m}$  becomes.

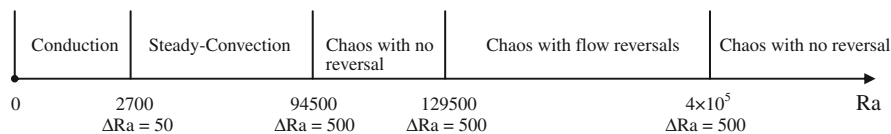


**Fig. 13.** Bifurcation diagram illustrating different flow regimes encountered in the loop and their existing ranges on the  $Ra$  axis.  $\Delta Ra$  is the maximum error associated with each transition.

ble convection, the chaotic regime characterized by flow reversals disappears and the flow rotates in one direction with small oscillations indefinitely, i.e. convection becomes stable again for a large enough Rayleigh number.

#### 4. Conclusions

Transient numerical simulations were performed in a water-filled thermal convection loop heated from below and cooled from above. The results are presented in terms of streamlines, isotherms, and local heat flux along the walls for different flow regimes encountered as the Rayleigh number increased from 1000 to 150,000. Detailed numerical simulations of the transitions taking place as the flow reversed direction during the chaotic regime were revealed for the first time by presenting the temporal evolution of the flow structure during these transitions, and by providing the temporal evolution of the mass flow rate and local heat flux at selected locations in the system.

The flow visualization over time showed that each transition begins with slight flow deformations observed in the vicinity of the temperature discontinuity. As the fluid neared a motionless state, a rising hot stream pushed the cold fluid against the old direction of rotation, leading to an unsteady-state with a new flow direction opposite to the previous one. The reversal onset was characterized by deformations taking the form of small circulations propagating along the wall away from the discontinuity and against the new direction of rotation, while new cells with higher intensity are created at the discontinuity. This behavior, which resembles the well-known Kelvin–Helmholtz instability, intensifies with time after the fluid velocities had dropped significantly. The time history of the heat flux distribution along the walls during flow reversals depicted a very complex distribution, characterized by long waves, in the central region of the walls and also near the discontinuities at both ends of the walls. These waves propagated in an organized fashion and seemed to predict the direction of the flow after the transition.

#### Acknowledgments

The authors thank Kameron Decker Harris, Floyd Vilmont, John Guckenheimer, and Sarah Iams for helpful discussions, and acknowledge support from the Vermont Advanced Computing Center (VACC) and NASA EPSCoR.

#### References

- [1] K.T. Yang, Natural convection in enclosures, in: S. Kakac et al. (Eds.), *Handbook of Single-Phase Heat Transfer*, Wiley, New York, 1987 (Chapter 13).
- [2] G.D. Raithby, K.G.T. Hollands, Natural convection, in: W.M. Rohsenow et al. (Eds.), *Handbook of Heat Transfer*, third ed., McGraw-Hill, New York, 1998 (Chapter 4).
- [3] Y. Jaluria, Natural convection, in: A. Bejan, A.D. Kraus (Eds.), *Heat Transfer Handbook*, Wiley, New York, 2003 (Chapter 7).
- [4] R. Greif, Natural circulation loops, *ASME J. Heat Transfer* 110 (1988) 1243–1258.
- [5] Y. Zvirin, A review of natural circulation loops in pressurized water reactors and other systems, *Nucl. Eng. Des.* 67 (1981) 203–225.
- [6] E.N. Lorenz, Deterministic nonperiodic flow, *J. Atmos. Sci.* 20 (1963) 130–141.
- [7] C. Sparrow, *The Lorenz Equations: Bifurcations, Chaos and Strange Attractors*, Springer, New York, 1982.
- [8] G. Desrayaud, A. Fichera, M. Marcoux, Numerical investigation of natural convection in a 2D-annular closed-loop thermosyphon, *Int. J. Heat Fluid Flow* 27 (2006) 154–166.
- [9] J.B. Keller, Periodic oscillations in a model of thermal convection, *J. Fluid Mech.* 26 (1966) 599–606.
- [10] P. Welander, On the oscillatory instability of a differentially heated fluid loop, *J. Fluid Mech.* 29 (1967) 17–30.
- [11] H.F. Creveling, J.F. De Paz, J.Y. Baladi, R.J. Schoenhals, Stability characteristics of a single-phase free convection loop, *J. Fluid Mech.* 67 (1975) 65–84.
- [12] M. Gorman, P.J. Widmann, K.A. Robins, Nonlinear dynamics of a convection loop: a quantitative comparison of experiment with theory, *Physica D* 19 (1986) 255–267.
- [13] P.K. Yuen, H.H. Bau, Optimal and adaptive control of chaotic convection—theory and experiments, *Phys. Fluids* 11 (1999) 1435–1448.
- [14] J. Tang, H.H. Bau, Stabilization of the no-motion state in Rayleigh–Bénard convection through the use of feedback control, *Phys. Rev. Lett.* 70 (1993) 1795–1798.
- [15] J. Tang, H.H. Bau, Feedback control stabilization of the no-motion state of a fluid confined in a horizontal, porous layer heated from below, *J. Fluid Mech.* 257 (1993) 485–505.
- [16] J. Tang, H.H. Bau, Stabilization of the no-motion state of a horizontal fluid layer heated from below with Joule heating, *ASME J. Heat Transfer* 117 (1995) 329–333.
- [17] J. Tang, H.H. Bau, Experiments on the stabilization of the no-motion state of a fluid layer heated from below and cooled from above, *J. Fluid Mech.* 363 (1998) 153–171.
- [18] J. Tang, H.H. Bau, Numerical investigation on the stabilization of the no-motion state of a fluid layer heated from below and cooled from above, *Phys. Fluids* 10 (1998) 1597–1610.
- [19] P.K. Vijayan, H. Austregesilo, Scaling laws for single-phase natural circulation loops, *Nucl. Eng. Des.* 152 (1994) 331–347.
- [20] P.K. Vijayan, Experimental observations on the general trends of the steady state stability behavior of single-phase natural circulation loops, *Nucl. Eng. Des.* 215 (2002) 139–152.
- [21] Y.Y. Jiang, M. Shoji, M. Naruse, Boundary condition effects on flow stability in a toroidal thermosyphon, *Int. J. Heat Fluid Flow* 23 (2002) 81–91.
- [22] Y.Y. Jiang, M. Shoji, Spatial and temporal stabilities of flow in a natural circulation loop: influences of thermal boundary condition, *ASME J. Heat Transfer* 125 (2003) 612–623.
- [23] A.S. Lavine, R. Greif, J.A.C. Humphrey, Three-dimensional analysis of natural convection in a toroidal loop: effect of tilt angle, *ASME J. Heat Transfer* 108 (1986) 796–805.
- [24] A.S. Lavine, R. Greif, J.A.C. Humphrey, A three-dimensional analysis of natural convection in a toroidal loop—the effect of Grashof number, *Int. J. Heat Mass Transfer* 30 (1987) 251–262.
- [25] E.A. Burroughs, E.A. Coutsias, L.A. Romero, A reduced-order partial differential equation model for the flow in a thermosyphon, *J. Fluid Mech.* 543 (2005) 203–237.
- [26] W. Ambrosini, N. Forgiione, J.C. Ferreri, M. Bucci, The effect of wall friction in single-phase natural circulation stability at the transition between laminar and turbulent flow, *Ann. Nucl. Energy* 31 (2004) 1833–1865.
- [27] D.S. Pilkhwal, W. Ambrosini, N. Forgiione, P.K. Vijayan, D. Saha, J.C. Ferreri, Analysis of the unstable behavior of a single-phase natural circulation loop with one-dimensional and computational fluid-dynamics models, *Ann. Nucl. Energy* 34 (2007) 339–355.
- [28] FLUENT Manual, FLUENT Inc., 10 Cavendish Court, Centerra Resource Park, Lebanon, NH 03766, USA, 2006.
- [29] T.H. Kuehn, R.J. Goldstein, An experimental and theoretical study of natural convection in the annulus between horizontal concentric cylinders, *J. Fluid Mech.* 74 (1976) 695–719.
- [30] P.G. Drazin, W.H. Reid, *Hydrodynamic Stability*, second ed., Cambridge University Press, UK, 2004 (Chapter 1).